Genesis and decay of baroclinic eddies in the seasonally ice-covered Arctic Ocean

GIANLUCA MENEGHELLO[1] *, JOHN MARSHALL[1], CAMILLE LIQUE[2], PÅL ERIK ISACHSEN[3,4],
EDWARD DODDRIDGE[1,5], JEAN-MICHEL CAMPIN[1], HEATHER REGAN[2], CLAUDE TALANDIER[2]

[1]*Massachusetts Institute of Technology, Cambridge, MA, USA.*
[2]*Univ. Brest, CNRS, IRD, Ifremer, Laboratoire d'Océanographie Physique et Spatiale (LOPS), IUEM, Brest, France*
[3]*University of Oslo, Oslo, Norway*
[4]*Norwegian Meteorological Institute, Oslo, Norway*
[5]*Institute for Marine and Antarctic Studies, University of Tasmania, Hobart, Tasmania, Australia*

ABSTRACT

Observations of ocean currents in the Arctic show a curious, and hitherto unexplained, vertical and temporal distribution of eddy kinetic energy. A marked seasonal cycle is found close to the surface: strong eddy activity during summer, observed from both satellites and moorings, is followed by very quiet winters. In contrast, subsurface eddies persist all year long within the deeper halocline and below. Informed by baroclinic instability analysis and a high resolution pan-Arctic ocean model, we explore the origin and evolution of baroclinic eddies in the seasonally ice-covered Arctic Ocean. Surface-intensified eddies are generated in the summer and decay in the winter when they are dissipated by friction against sea ice. Meanwhile deeper eddies, which obtain their energy from the halocline, are less susceptible to the seasonal cycle. We show how mesoscale activity is fundamentally different between ice-covered and ice-free regions, with important consequences for the evolution of the Arctic eddy field under a changing ice cover and stratification.

1. Introduction

In the global ocean, mesoscale eddies account for most of the turbulent kinetic energy (Wunsch 2002) and are key to the equilibrium of the large-scale circulation (Marshall et al. 2002; McWilliams 2008), ocean ventilation of tracers (MacGilchrist et al. 2017), upper-ocean biology (Watanabe et al. 2014) or pollutant dispersion (Marta-Almeida et al. 2013). In the Arctic basin, however, in-situ observations taken under sea ice (Timmermans et al. 2012), observationally constrained estimates of eddy fluxes (Meneghello et al. 2018b), and results from simulations at high resolution (Regan et al. 2020), suggest a lack of energy at the mesoscale in the Arctic interior compared to characteristic midlatitude ocean dynamics. The usual ingredients generating mesoscale ocean turbulence may be inefficient in the Arctic, owing to the presence of a sea ice governor diminishing the rates of Ekman pumping (see Meneghello et al. (2017, 2018a, 2019); Dewey et al. (2018); Zhong et al. (2018)) and hence the creation of potential energy stored in the halocline. Moreover, the strong stratification is not diffused away due to extremely low levels of vertical mixing (Lique et al. 2014).

That said, mesoscale eddies are a ubiquitous feature of the Arctic Ocean. Recent satellite observations (Kozlov et al. 2019) have identified an active surface eddy field in ice-free regions and in the marginal ice-zone. But these observing systems cannot provide information within the ice covered regions or about the eddy structure at depth. Observations of temperature and salinity profiles (Zhao et al. 2014, 2018) from Ice-Tethered Profilers (ITP, Toole et al. (2011)) and the BGEP moorings have begun to characterize the eddy field below the surface, but such in-situ observations remain sparse in space and time. Despite recent improvements, the presence of sea ice and the difficulties of accessing this remote region has led to a rather patchy description of the mesoscale field in the Arctic which lacks the detailed quantification available at the surface of other oceans (e.g., Le Traon 1991).

This lack of observability, together with the challenge of numerical simulation in the Arctic (owing, for example, to the small deformation radius (Nurser and Bacon 2014) and the need to represent the complexity of ocean-sea ice interaction) has limited our ability to apprehend the nature and role of the mesoscale in the general circulation of the Arctic. For example, although we observe eddy transport of heat and freshwater in the interior of the Arctic basins (Våge et al. 2016), we do not understand the details of the eddy generation process (Zhao et al. 2014) and if mesoscale activity is fundamentally different be-

---

*Corresponding author address: Department of Earth, Atmospheric and Planetary Sciences, Massachusetts Institute of Technology, Cambridge, Massachusetts 02139-4307, USA.
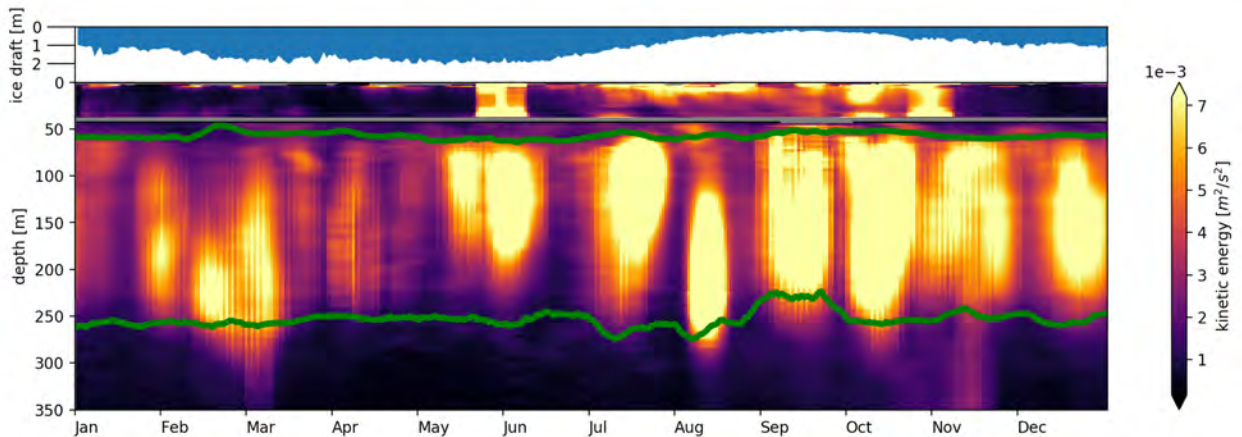E-mail: mgl@mit.edu

FIG. 1. 2003-2018 climatology of observed kinetic energy at 75°N, 150°W in the central Canada basin (see black mark in Figure 2). Two separate depth ranges of enhanced kinetic energy are visible, bounded by peaks in stratification N^2 at approximately 50 m and 250 m depth (green lines, see also Figure 3). The blue curve in the top panel shows observed ice draft (inverted y axis), changing together with the seasonality in the surface layer kinetic energy (the spike in kinetic energy level at the end of May corresponds to a single event in May 2017, see Figure 12 for a time resolved version of the same data). The gray band at approximately 40 m depth corresponds to the location of the mooring buoy, and separates observations based on Acoustic Doppler Current Profiler (ADCP) above and McLane Moored Profiler (MMP) below. Ice draft observations are based on an Upward-Looking Sonar (ULS). Data from mooring A of the Beaufort Gyre Exploration Project (http://www.whoi.com/beaufortgyre).
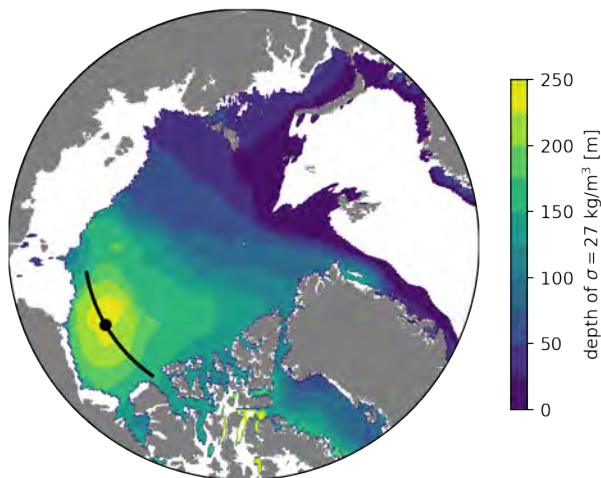

FIG. 2. Depth of the $\sigma = 27 \, \mathrm{kg \, m}^{-3}$ isopycnal. The black circle marks the mooring location at 75°N 150°W. The black line marks the section corresponding to Figure 3 and Figure 10.

tween ice-covered and ice-free regions. The eddies' origin itself remains a subject of debate: are they generated only within the relatively fast and unstable coastal currents, from where they can be advected into the central Arctic, or is the entire Arctic baroclinically unstable?

In this work we address the origin and seasonal evolution of eddies in the central Arctic. In section 2 we present observations of kinetic energy in the Canada Basin over the seasonal cycle. In section 3 we interpret those observations using linear baroclinic instability theory to explore the combined effect of stratification and friction at the ice-ocean interface on the development of baroclinic eddies. We show how the peculiar vertical structure of the eddy field is generated, and discuss how its variability is connected with the seasonal cycle of ice cover. In section 4 we use a high resolution, pan-Arctic numerical model to explore the same mechanisms over the entire Arctic. In section 5 we discuss and conclude.

2. Observations of eddies in the Arctic

Figure 1 shows a 2003-2018 seasonal climatology of kinetic energy measured in the central Canada basin at 75°N, 150°W (see black mark in Figure 2). Clearly visible are two layers of enhanced kinetic energy, delimited by two peaks in the background stratification $N^2 = -\frac{g}{\rho_0}\frac{\partial \rho}{\partial z}$ (green lines). As shown in Figure 3, these peaks separate the halocline, containing mostly Pacific waters, from a surface layer containing mostly meteoric and ice-melt water above, and a deep layer of largely Atlantic origin below.

The presence of subsurface intensified eddies in the halocline was first reported in the 1970s (Newton 1973; Newton et al. 1974; Hunkins 1974; Manley and Hunkins 1985) and has been recently addressed by Timmermans et al. (2008) and Zhao et al. (2014); Zhao and Timmermans (2015); Zhao et al. (2016, 2018). In particular, Zhao et al. (2018) connect the vertical distribution of eddy kinetic energy with the vertical structure of the stratification by partitioning the observed kinetic energy onto the neutral modes of the observed stratification profile. They

show how a large part of the eddy kinetic energy is contained in the second neutral baroclinic mode, characterized by a subsurface maximum.

Another feature visible in Figure 1 is the contrast between a marked seasonal cycle in the surface layer, down to a depth of 30 m to 40 m, and the more persistent high level of kinetic energy within the deeper halocline. In the surface layer, the summer elevated kinetic energy level and the very quiet winters are apparently closely linked to the seasonal cycle in sea ice draft, shown by the blue shading in the top panel.

3. Baroclinic instability and eddy dissipation in a seasonally ice covered ocean

The available potential energy stored in the sloping density surfaces of the halocline, provides a ready source of energy for baroclinic instability (BI). But, in order for it to be extracted, conditions for BI must be met. Baroclinic instability can result from the interaction between buoyancy gradients at the surface and at the bottom of the ocean, as described by Eady (1949), from the interaction between a buoyancy gradient at one boundary and an interior potential vorticity gradient, as described by Charney (1947), or from a change in sign in the interior potential vorticity gradient (Phillips 1954). [See also Charney and Stern (1962); Pedlosky (1964); Smith (2008) for a description of the conditions required for BI to develop]. However, along with energy sources, there are many energy sinks, associated with, for example, frictionally driven Ekman layers at the surface and the bottom (Charney and Eliassen 1949; Barcilon 1964; Williams and Robinson 1974). We shall find that the presence of sea-ice at the surface can strongly damp the growth of BI.

The influence of ocean-ice friction on the development of baroclinic eddies in the ice-covered Arctic has been previously addressed by Hunkins (1974) and Manley and Hunkins (1985), who performed a stability analysis based on stratification and velocity profiles exponentially decaying with depth (Hunkins 1981). Based on their analysis, Manley and Hunkins (1985) reported that "when the [baroclinic instability] theory is applied to the central Arctic Ocean, using representative oceanographic parameters, it is found that when a rigid lid [no-slip boundary condition] is assumed, the ocean is stable and no amplification of disturbances takes place. Thus if baroclinic instability is the cause [of eddy generation], it must occur in some other location where conditions are less stable". At the same time, Ou and Gordon (1986) and Chao and Shaw (1996) showed that preexisting eddies, for example generated in unstable ice-free regions, are dissipated on a time scale of the order of days once advected below ice (see also Section 3c below). Hence, contrary to the observational evidence of Figure 1, previous theoretical considerations suggest that no baroclinically-generated eddies should be expected in the ice-covered Arctic Ocean. How can theory and observations be reconciled?

Our analysis starts from the linearized quasi-geostrophic potential vorticity (PV) equation

$$\frac{Dq}{Dt} = -\boldsymbol{u} \cdot \nabla Q \tag{1a}$$

$$q = \nabla^2 \psi + \frac{\partial}{\partial z}\left(\frac{f_0^2}{N^2}\frac{\partial \psi}{\partial z}\right) + \beta_0 y \tag{1b}$$

where q is the perturbation potential vorticity, f_0 is the Coriolis parameter, β_0 is its gradient, N^2 is the stratification and $\psi = \frac{p}{\rho_0 f_0}$ is the perturbation streamfunction, with p being pressure and ρ_0 a reference density, so that $\boldsymbol{u} = -\hat{k} \times \nabla \psi$. The total derivative $\frac{D}{Dt} = \left(\frac{\partial}{\partial t} + \boldsymbol{U} \cdot \nabla\right)$ is based on the background velocity $\boldsymbol{U}$, and ∇Q is the background potential vorticity gradient.

Boundary conditions for (1) are provided at the ice-ocean interface and at the ocean floor by imposing the quasi-geostrophic density equation (Cushman-Roisin and Beckers 2010, eq. 16.13) and matching the interior vertical velocity to the Ekman pumping w_E, itself driven by the geostrophic relative vorticity via $w_E = \pm\frac{d}{2}\nabla^2\psi$ where the d is the Ekman layer depth and the sign is positive at the ocean floor and negative at the surface (Cushman-Roisin and Beckers 2010, eq. 8.27)

$$\frac{D}{Dt}\left(\frac{\partial \psi}{\partial z}\right) = \frac{\partial \boldsymbol{U}}{\partial z} \cdot \nabla \psi \pm \frac{N^2}{f_0}\underbrace{\frac{d}{2}\nabla^2\psi}_{w_E}. \tag{2}$$

Note that we are here neglecting the vertical velocity due to the flow crossing a non-flat bottom, whose effect has been analyzed by Manucharyan and Isachsen (2019).

At the scales at which the background potential vorticity Q is computed, the relative vorticity term $\nabla^2\Psi$, where Ψ is the background streamfunction, is two orders of magnitude smaller than the stratification term $\frac{\partial}{\partial z}\left(\frac{f_0^2}{N^2}\frac{\partial \Psi}{\partial z}\right)$ and can be neglected in the computation of the background potential vorticity

$$Q = \nabla^2\Psi + \frac{\partial}{\partial z}\left(\frac{f_0^2}{N^2}\frac{\partial \Psi}{\partial z}\right) + \beta_0 y \tag{3}$$

We recall how the dynamics described by (1) and (2) can also be interpreted in terms of the organization of isopycnal slopes. The vertical velocity shear $\frac{\partial \boldsymbol{U}}{\partial z}$ on the right hand side of (2) can be related to vertical and horizontal variations in the large-scale density field by the thermal wind relation

$$\frac{\partial \boldsymbol{U}}{\partial z} = \frac{g}{f_0 \rho_0}\frac{\partial \rho}{\partial z}\hat{k} \times \nabla z_\rho = -\frac{N^2}{f_0}\hat{k} \times \nabla z_\rho \tag{4}$$
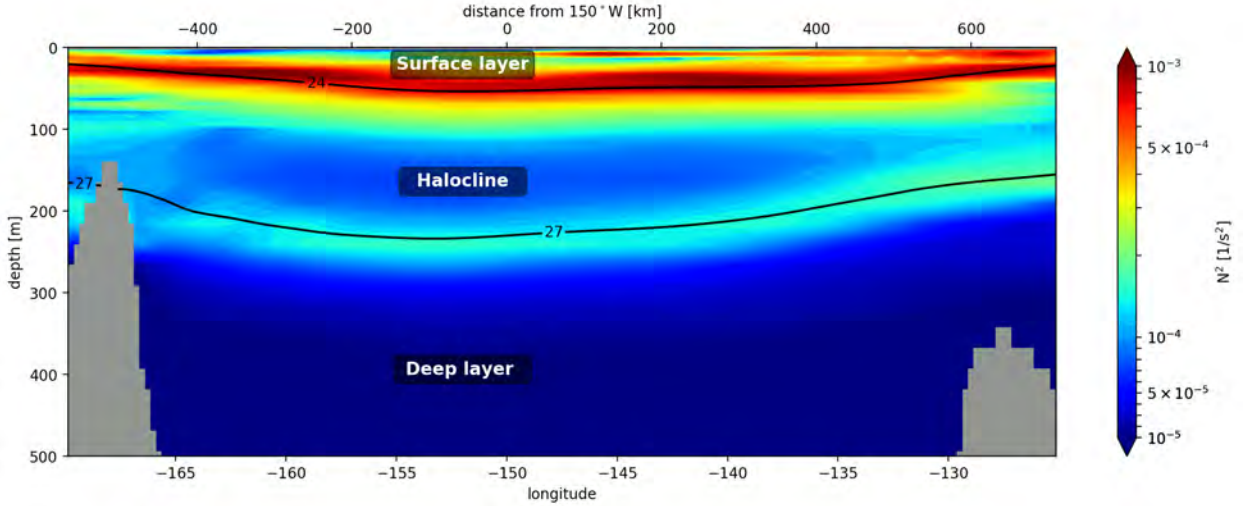
FIG. 3. Stratification $N^2 = -\frac{g}{\rho_0}\frac{\partial \rho}{\partial z}$ across the Canada basin at 75°N (see black line in Figure 2). Note the two peaks in stratification at approximately 50 m and 200 m depth extending across the Canada basin. Black contours mark the $\sigma = 24\,\mathrm{kg\,m^{-3}}$ and $\sigma = 27\,\mathrm{kg\,m^{-3}}$ isopycnals. Data based on the 2005-2017 World Ocean Atlas climatology.

where ∇z_ρ is the isopycnal slope. Similarly, the second term in the PV gradient (3) can be rewritten using (4) as

$$\nabla \frac{\partial}{\partial z}\left(\frac{f_0^2}{N^2}\frac{\partial \Psi}{\partial z}\right) = f_0 \hat{\boldsymbol{k}} \times \frac{\partial}{\partial z}\nabla z_\rho \qquad (5)$$

and depends on the vertical variation of the isopycnal slope rather than on the isopycnal slope itself.

The solution of (1) with boundary conditions (2) depends on the particular choice of the background stratification N^2 and velocity profile $\boldsymbol{U}$, and this is where our analysis differs from the one carried out by Hunkins (1981). As we will show, the choice of a more realistic stratification has important consequences for our ability to explain the observations presented in Figure 1.

Specialization to the Arctic. To specialize our BI problem to the Arctic, we:

- set β_0 to zero,

- choose a reference system aligned with the flow, so that $\boldsymbol{U} = (U, 0)$,

- choose reference stratification and current profiles motivated by Arctic observations,

- parameterize the interaction of eddies with the ice by employing an Ekman layer at the upper boundary, as in equation (2), and

- assume that the bottom is flat.

Our reference stratification N^2 and velocity profile U are shown as solid black lines in Figure 4a and Figure 4c.

While idealized, they closely match the stratification and velocity computed using salinity and temperature from the 2005-2017 World Ocean Atlas (WOA) climatology, shown as thick gray lines. In particular, our reference stratification profile is designed to mimic the two-peak structure characterizing the density structure within the Canada basin (see also Figure 3). Our reference velocity profile, obtained by fitting an exponential curve to the current's speed profile computed from the WOA climatology using the thermal wind relation (4) (thick gray line), has a maximum surface velocity of approximately $2\,\mathrm{cm\,s^{-1}}$, and decays with depth on a length scale of approximately 200 m. This is the same velocity profile used by Hunkins (1981) in his baroclinic instability analysis. The choice of a more complex velocity profile, including the inflection points characterizing the WOA-derived velocity at approximately 25 m, 150 m and 250 m, introduces additional instabilities which do not provide any further insight to the physics discussed in this work. Accordingly, we omit them from our discussion; the only difference with respect to the analysis of Hunkins (1981) is in our choice of stratification.

Also shown in the central panel of Figure 4 is the quasi-geostrophic PV gradient, computed from the imposed stratification N^2 and velocity profile U using (4) and (5). As we will see, the PV gradient reversal within the halocline plays a central role in facilitating the growth of halocline eddies through the right hand side of (1a). We also remark that this is exactly the ingredient missing in the analysis of Hunkins (1981). Despite the more interesting, exponetially decaying current and stratification profiles assumed by Hunkins (1981) in-lieu of the linear and
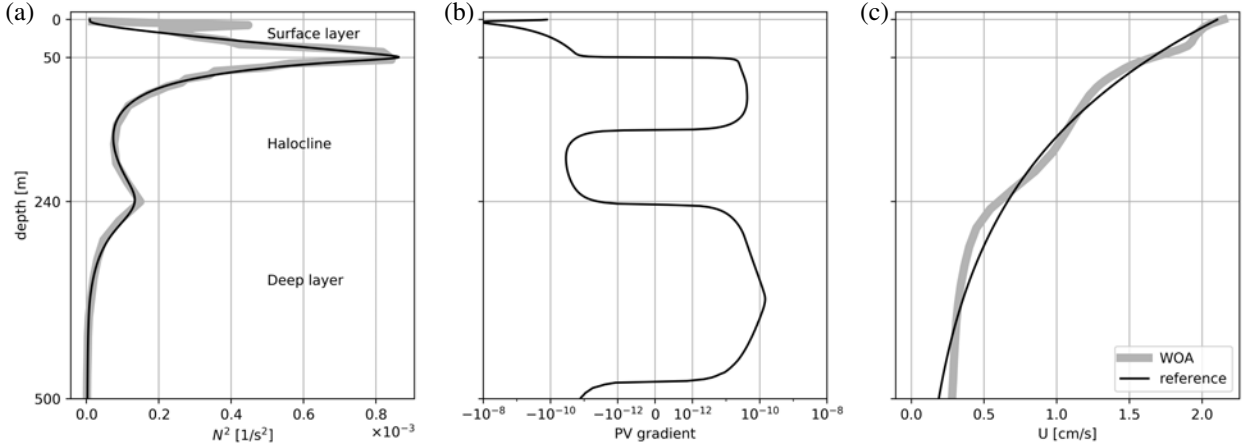
FIG. 4. Reference profiles of stratification $N^2 = -\frac{g}{\rho_0}\frac{\partial \rho}{\partial z}$ (left, black) and current speed (right, black) used for the baroclinic instability analysis. The central panel shows the corresponding quasi-geostrophic potential vorticity gradient. Gray thick lines shows profiles computed from salinity and temperature fields from the 2005-2017 World Ocean Atlas climatology at 75°N, 150°W. Both stratification and velocity profiles extend from the surface to the ocean floor at a depth of 3800 m, but only the top 500 m are shown here.

constant profiles of Eady (1949), Hunkins (1981) problem can still be thought as a "generalized Eady problem" in which the right hand side of (1) is zero and the only instability allowed are due to interacting top and bottom edge waves.

Once a stratification and velocity profiles have been chosen, the growth rate, phase speed and vertical structure of the perturbations can be obtained by numerically solving the generalized eigenvalue problem obtained from (1) with boundary conditions (2). A separation of variables is assumed of the form:

$$\psi = \hat{\psi}(z)\,e^{i(kx-\omega t)}, \qquad (6)$$

where ω is the complex frequency and k the longitudinal wavenumber. We refer the reader to Smith (2008); Tulloch et al. (2011); Isachsen (2011, 2015); Trodahl and Isachsen (2018) for details on the solution of the eigenvalue problem. A constant bottom friction is included in all computations by setting $d = 50$ m at the ocean floor in (2). The Coriolis parameter f_0 is set to $1.4 \times 10^{-4}\,\text{s}^{-1}$ and its gradient β_0, very small in the Arctic, is set to zero. The results presented below do not change appreciably for d in the range 0 m to 100 m at the ocean floor, or for values of β_0 different from zero but characteristic of the Arctic Ocean.

Results of our linear instability analysis are summarized in Figure 5 for selected values of the surface Ekman layer depth d. They will be discussed next by first considering the effect of stratification in the absence of surface friction, and then adding the effect of friction against sea ice.

a. Effect of stratification

We start by analyzing the effect of stratification by considering the ice-free, frictionless ($d = 0$ m in (2)) case. The growth rates of all unstable modes are plotted as a function of the wavenumber in Figure 5a (thick lines). Three different branches can be identified, marked with blue, green and red. For each branch, the vertical structure of the mode $|\hat{\psi}|$ corresponding to the fastest growing wavenumber is plotted with thick lines and matching colors in Figure 5b: a surface-intensified mode (blue), a halocline-intensified mode (green) and a deep-intensified mode (red) can be readily identified, the latter decaying monotonically with depth down to the ocean floor at 3800 m (not shown).

The surface mode (blue) grows on a time scale of order ten days, and is characterized by a phase speed of order $2\,\text{cm s}^{-1}$ and a horizontal length scale of order 100 m. Its signature is concentrated between the surface and the shallower peak in stratification located at 50 m depth (see inset in Figure 5b). The halocline mode (green) is characterized by a slower time scale of order two months, a phase speed of order $1\,\text{cm s}^{-1}$ and a larger horizontal length scale of order 10 km; its signature reaches its maximum in the halocline between the two peaks in stratification at 50 m and 240 m, but in the absence of friction its imprint is still visible at the surface. The deep mode (red), while characterized by similar time and length scales, has a much slower phase speed of order $1\,\text{mm s}^{-1}$, its maximum lies below the deepest peak in stratification, and decays to zero across the halocline before reaching the surface.

As shown by Zhao et al. (2018) in their computation of neutral modes, the stratification's vertical structure is at the origin of the development of three different modes. By performing a stability analysis in-lieu of the neutral mode
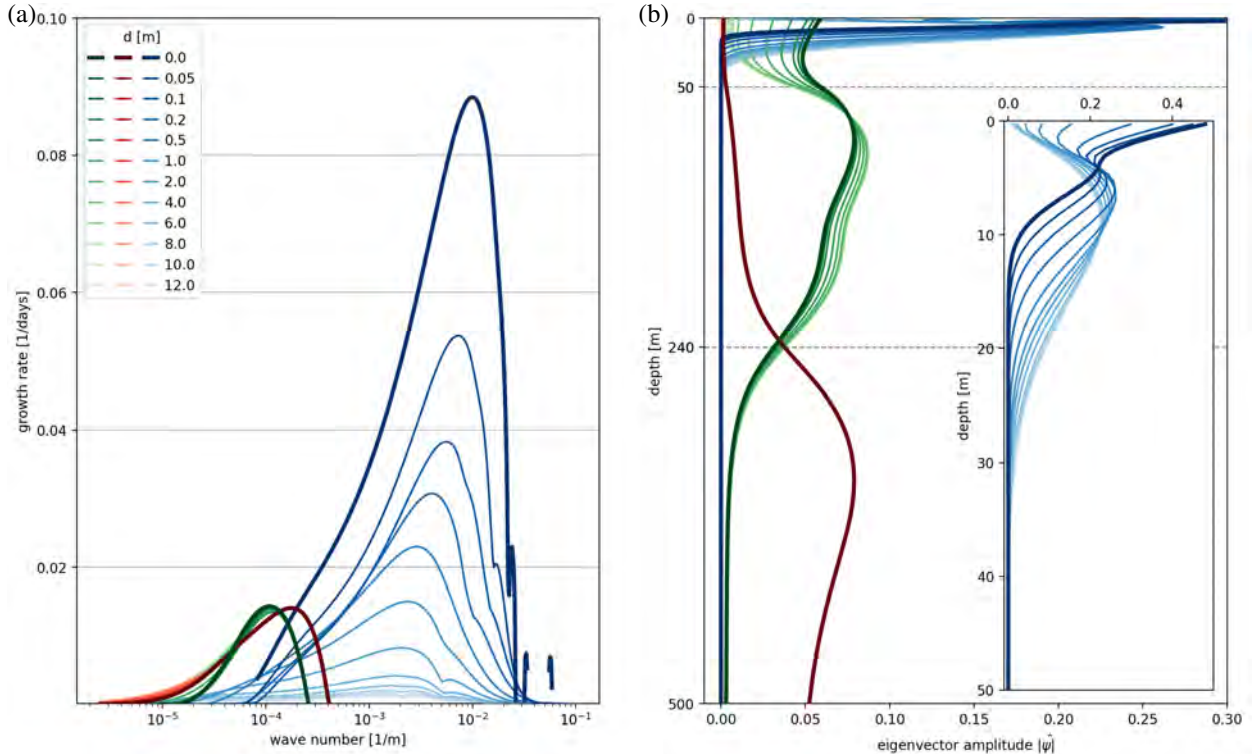
FIG. 5. Growth rate (left) and vertical structure $|\hat{\psi}|$ of the fastest growing wavenumbers (right) for the three unstable branches. Blue is for the surface mode, green for the halocline mode, red for the deep mode. Shades of the same color denote different values of surface friction or, equivalently, different Ekman layer depths d. The inset in the right panel shows the surface mode in the top 50 m. Gray dashed lines mark the location of the peaks in N^2.

decomposition done by Zhao et al. (2018), we have here identified growth rates and phase speeds for each mode. It is important to note that the three modes grow independently, at different depths, and with different characteristic growth rates and horizontal length scales.

The modes' vertical structure is remarkably consistent with the picture of the kinetic energy field shown in Figure 1: independent perturbations grow in the surface layer and within the halocline. Deeper eddies, laying below the 240 m peak and corresponding to the deep mode (red), are not shown in the climatology of Figure 1 but can be seen in Figure 12 (see, e.g., October 2012, and February and July 2013) and have been observed in other mooring- and ITP-based observations (see, e.g. Figure 3 in Zhao and Timmermans 2015).

While we have shown that different perturbations can grow independently at different depths, we have not yet explained the strong seasonality of the surface eddies. To understand the origin of this seasonality, we need to introduce friction at the surface.

b. Effect of friction on the growth of perturbations

To explain the relationship between ice draft and surface eddy activity suggested by Figure 1, we now introduce the frictional effects due to the presence of the ice cover. In our model, the surface Ekman layer depth d is a proxy for the ice's ability to sustain internal stress, itself showing a very large variability over the seasonal cycle. In the limit of negligible friction just discussed ($d = 0$ m), which can be interpreted as representing the ice-free summer, we recover the free-slip boundary condition characterizing the baroclinic instability problem of Charney (1947) and Eady (1949). As the Ekman layer depth increases during autumn and winter, the dissipation of vorticity by the second term on the right hand side of (2) increases and the growth rate decreases, as shown by Williams and Robinson (1974) and Hunkins (1981). For large values of d the vorticity is driven to zero at the surface.

Observational estimates of Ekman layer depths in the Arctic suggest a median value of order $d \approx 11$ m (see, e.g., Figure 5 of Cole et al. 2014) or, equivalently, a vertical diffusivity $\nu_E = \frac{d^2 f_0}{2}$ of almost 10^{-2} m^2 s^{-1}. We then analyze the effect of viscosity by varying the Ekman layer depth between 0 m and 12 m. The obtained growth rates
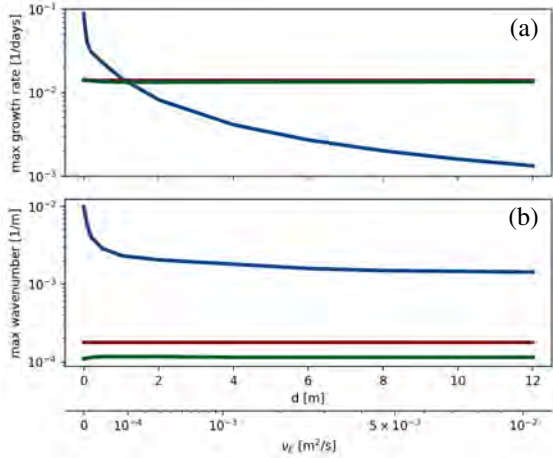
FIG. 6. Growth rate and wavenumber of the fastest growing perturbation as a function of the Ekman layer thickness d or, equivalently, of the vertical diffusivity $\nu_E = \frac{d^2 f_0}{2}$. Colors as in Figure 5. The green and red curves in panel (a) are almost indistinguishable.

FIG. 7. Growth rate and wavenumber of the fastest growing perturbation as a function of the maximum stratification N^2. Colors as in Figure 5.

and vertical structure of the perturbations are shown for selected values of d in Figure 5 in shades of blue, green and red, and the dependence of the growth rate and the fastest growing wavenumber on d is summarized in Figure 6. Even for small Ekman layer depths, friction has a strong effect on both the growth rate and length scale of the surface mode (blue). An Ekman layer depth of 2 m ($\nu_E \approx 3 \times 10^{-4}\,\mathrm{m^2\,s^{-1}}$) is enough to reduce the growth rate by more than an order of magnitude, with higher friction dampening the perturbation growth even more (Figure 6a, blue). At the same time, the fastest growing horizontal length scale increases from 100 m for the ice free case ($d = 0$ m) to almost 1 km for $d = 10$ m ($\nu_E \approx 7 \times 10^{-3}\,\mathrm{m^2\,s^{-1}}$) (Figure 6b, blue). The vertical structure of the surface mode shows the effect of dissipation. Increasing friction drives the mode to zero at the surface, and a subsurface peak in the streamfunction amplitude is developed, but is still contained in the surface layer, as can be seen in the inset of Figure 5b.

The strong effect of friction on the surface mode should be contrasted with its effect on the halocline (green) and the deep (red) modes. Their growth rate and fastest growing length scale are barely affected by increased friction, as seen in Figure 5a and Figure 6. The only visible effect is a reduction in the surface amplitude of the halocline modes (Figure 5b), but the bulk of the perturbations, lying within the halocline below the stratification peak at 50 m, is unchanged.

Note how the growth rate of the surface mode is of the same order as for the halocline and the deep modes for an Ekman layer of order 1 m, while being ten times larger in the ice-free, $d = 0$ m case, and ten times smaller for $d = 10$ m. As suggested by the climatology of kinetic en-
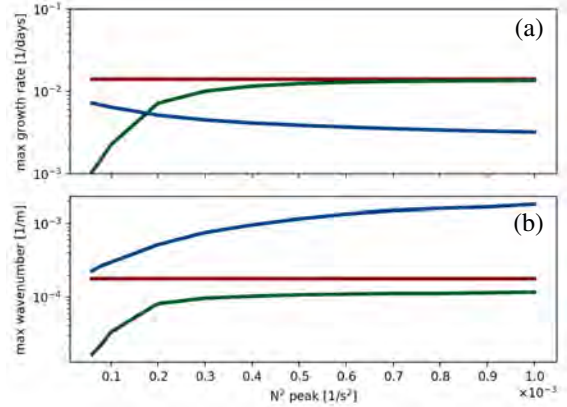
ergy in Figure 1, the growth of modes in the surface layer is strongly affected by interaction with the ice, with even small friction reducing growth rates by an order of magnitude or more.

The insulation of the halocline mode from the effect of friction against the ice cover depends on the presence of a strong stratification close to the surface. To understand how important this is, it is worth to repeat our baroclinic instability computations by varying the intensity of the surface peak in stratification from $10^{-3}\,\mathrm{s^{-2}}$, a value characteristic of the observed profile, to $10^{-4}\,\mathrm{s^{-2}}$, slightly less than the value of the deeper peak at 240 m, while keeping the Ekman layer depth fixed at 5 m. As can be seen in Figure 7, both the growth rate and wavenumber of the halocline mode (green) are affected once the stratification drops below approximately $6 \times 10^{-4}\,\mathrm{s^{-2}}$. For decreasing stratification, the model's halocline is only partially insulated from the ice above.

c. Effect of friction on preexisting eddies

How about preexisting eddies generated, e.g., in ice free regions during summer? Their spindown time scale can be estimated by energetic consideration as (Pedlosky 1992, Section 4.3)

$$T_\nu = \frac{K}{\dot{W}} = \frac{H}{d} f^{-1} \qquad (7)$$

where K is the kinetic energy of the eddy, $\dot{W}$ is the power dissipated by friction within the Ekman layer, H is the depth of the eddy and d is the Ekman layer length scale. If we consider a vertical scale $H \approx 50$ m, characterizing the surface layer, and an Ekman layer depth of order 1 m, the resulting time scale is about 4 days, with larger Ekman layer depths resulting in even faster dissipation times. This precludes the possibility of eddies traveling long distances within the surface layer while in contact with the ice cover: even an eddy with a relatively high phase speed
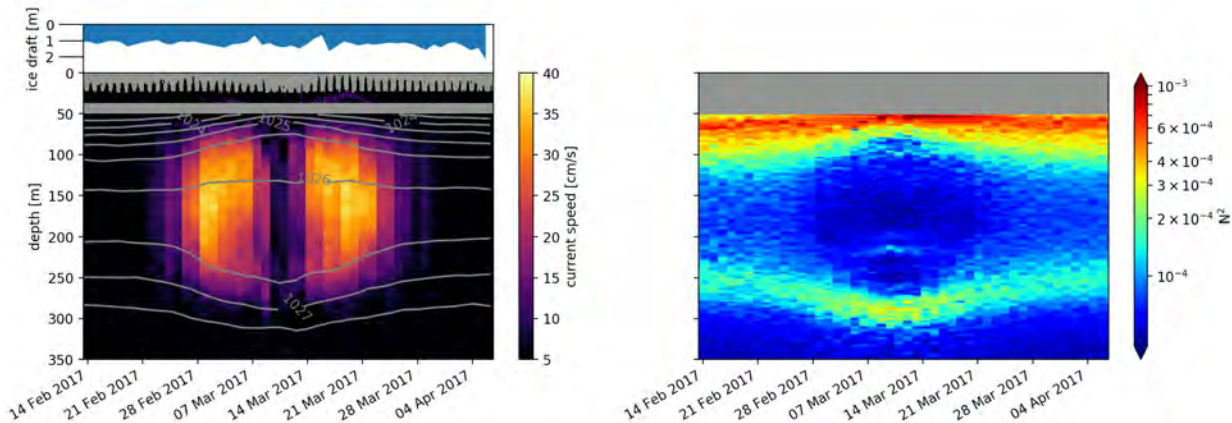
FIG. 8. Left: mooring observation of current speed and isopycnals (gray lines at $0.5\,\mathrm{kg\,m^{-3}}$ spacing) for an anticyclonic eddy passing by the mooring in winter 2017. Ice draft is shown in blue. See Figure 12 for kinetic energy. Right: stratification N^2. Gray regions denote missing data.

of $5\,\mathrm{cm\,s^{-1}}$ would move by less than $20\,\mathrm{km}$ in four days before being dissipated by an Ekman layer only $1\,\mathrm{m}$ deep.

In contrast, halocline and deep eddies are insulated from the ice by the strong stratification at each peak in N^2. This inhibits the vertical velocity — in a way qualitatively similar to the free-slip boundary condition $w_E = 0$ (i.e., (2) for $d = 0\,\mathrm{m}$) — and allows the perturbation driven by the interior potential vorticity gradient to decay by inviscid thermal wind. If the stratification N^2 is strong enough, the displacement in isopycnal depth induced by the passing eddy is sufficient to drive the velocity to zero before reaching the ice at the surface. This situation is exemplified in Figure 8, where we show mooring-based current speed observations of a subsurface, anticyclonic eddy during the winter of 2017 (see also Figure 12 for other similar cases). The eddy appears unaffected by the presence of thick sea ice (blue filled curve) during its one month-long transit. Indeed, a velocity shear, driven by the displacement of the isopycnal (gray lines) in combination with the strong stratification (right panel), reduces the current speed to zero already at a depth of $50\,\mathrm{m}$. No Ekman layer, and no frictional dissipation, is induced by the passing eddy, which can then move undisturbed under ice.

4. Pan-Arctic model

We have shown how a realistic stratification profile, combined with friction at the ice-ocean interface results in a halocline which is baroclinically unstable all year, and a surface layer where eddies are generated and dissipated over the seasonal cycle. In order to gain further insights on the spatial and temporal evolution of the eddy field in the Arctic as a function of the ice cover, we now resort to a Pan-Arctic, high resolution model.

Here we use results from a simulation based on the CREG12 configuration (Dupont et al. 2015), encompassing the Arctic and parts of the North Atlantic. It is based

on the NEMO (Madec and NEMO Team 2014) and LIM3 (Rousset et al. 2015) numerical models for the ocean and sea ice components, respectively. LIM3 uses an EVP (Elasto-Viscous-Plastic) rheology (Hunke and Dukowicz 1997). The configuration has a high vertical (75 levels) and horizontal (3-4km) resolution in the Arctic Ocean and is thus partially eddy resolving in the interior of the basin away from the shelves — see Figure 2 of Dupont et al. (2015) for details on the eddy resolving abilities of the model. The simulation used in the present study runs from 1979 to 2014. The forcing data set is the Drakkar forcing set 5.2 (which is an updated version of the fields described in Brodeau et al. (2010)). More details about the numerical design as well as representation of the mesoscale activity in the Arctic basin can be found in Regan et al. (2020).

The model allows us to further investigate if the ideas outlined so far apply to the entire Arctic. Figure 9 shows winter, summer and autumn snapshots of relative vorticity at $17\,\mathrm{m}$ (left) and $97\,\mathrm{m}$ (right) depth. The central Arctic is completely ice covered during winter, and characterized by low ice concentration or ice-free conditions during summer (purple, green and yellow contours). The intensity of the surface eddy field closely follows the ice concentration contours. Vorticity increases by more than four orders of magnitude between winter (top panel) and summer (middle panel, note the logarithmic color scale). As sea ice advances southward at the onset of autumn (bottom panels), the summer-generated eddies are dissipated and the central Arctic can be divided in an ice-free area characterized by an intense surface eddy field, and an ice-covered area with virtually no surface eddies: relative vorticity decays by more than four orders of magnitude across the marginal ice zone. The contrast with the vorticity field at $97\,\mathrm{m}$ depth (right panels) is stark: the well developed halocline eddy field is unaffected by the presence of ice. An animation of the vorticity field

SURFACE LAYER   HALOCLINE

WINTER

SUMMER
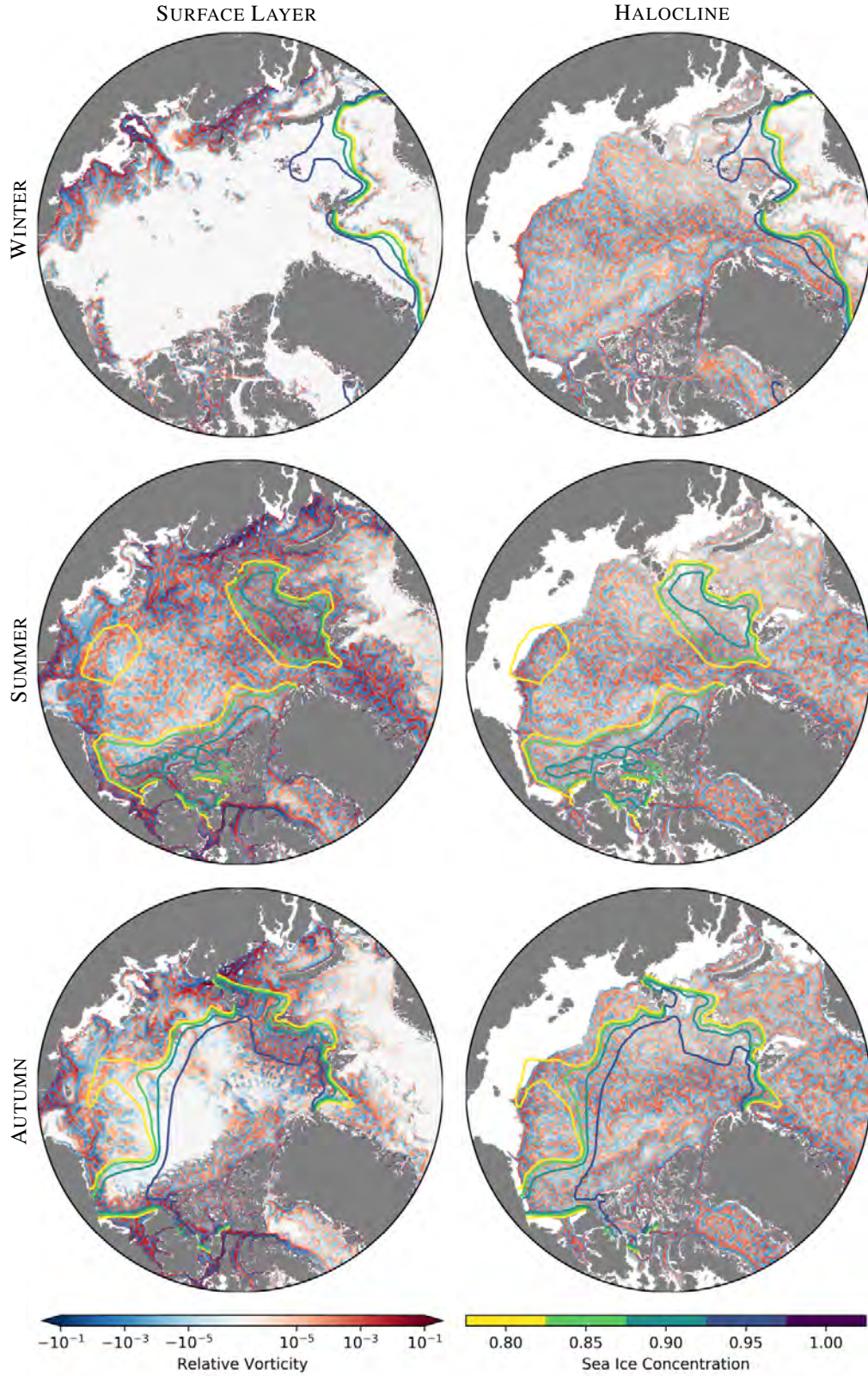
AUTUMN

Relative Vorticity   Sea Ice Concentration

FIG. 9. Relative vorticity (normalized by f_0) at 17 m (left) and 97 m (right) depth for the 2003 winter maximum (top) and summer minimum (middle) ice extension, and during autumn's ice formation (bottom); note the logarithmic color scale for the vorticity. Ice concentration contours range from 95% (blue) to 80% (yellow), every 5%. The model is not eddy resolving in the Barents sea (see Figure 2 of Dupont et al. (2015) for details). A time resolved animation is provided as supplemental material.

shown in Figure 9 is provided in Supplemental Material (`http://mgl.mit.edu/video/nemoEddies.mp4`).

5. Discussion and conclusions

Despite being a relatively quiet ocean, the Arctic Ocean hosts a ubiquitous mesoscale eddy field. Such activity is characterized by a peculiar vertical distribution of eddy kinetic energy, shown by the climatology in Figure 1. A marked seasonal cycle is found close to the surface: strong eddy activity during summer, captured by both remote and in-situ observations, is followed by very quiet winters. In contrast, subsurface intensified eddies persist all year long within the deeper halocline, and below.

We have addressed the origin and seasonal variability of the Arctic eddy field, and attempted to explain the prevalence of halocline, subsurface-intensified eddy activity characterizing the ice-covered interior Arctic Ocean. Our stability analysis, summarized by Figure 5, shows how the central Arctic is baroclinically unstable despite the presence of sea ice. This conclusion contrasts with previous analysis (Hunkins 1981; Manley and Hunkins 1985) who suggested that frictional dissipation against the ice cover would prevent baroclinic eddies from developing.

The only additional ingredient of our analysis with respect to the one performed by Hunkins (1981) is the more realistic stratification, shown in Figure 4, used in-lieu of the exponentially decaying profile. The resulting PV gradient inversion within the halocline, shown in the central panel of Figure 4, or, equivalently, the variations of isopycnal slope with depth (see equation (5)), enables the instability (through the right hand side of equation (1a)). Indeed, if the PV gradient in the interior is zero — corresponding to constant, but not necessarily zero, isopycnal slope — our baroclinic analysis returns only a surface intensified mode extending from the surface to the ocean floor and due to interacting top and bottom edge waves, as shown in Figure 11 and in agreement with the results of Hunkins (1981). A section mapping the PV gradient within the Canada Basin (Figure 10) shows PV reversals extending throughout the entire halocline. Baroclinic eddies can develop locally, and independently of the presence of sea-ice, everywhere within the halocline, rather than being generated in coastal areas and transported into the interior. At the same time, the growth rate of these halocline perturbations is of the order of months. In agreement with evidence from observations and models (Timmermans et al. 2012; Meneghello et al. 2017; Regan et al. 2020), only moderate eddy activity is to be expected: such growth rates are much smaller than the ones characterizing the surface layer of an ice-free ocean which can be ten times faster (see Figure 6).

Importantly, our analysis provides a dynamical interpretation for the observed seasonal variability shown in Figure 1. Surface eddies are strongly affected by the presence of ice cover, with even moderate friction reducing growth rates by two orders of magnitude and increasing the characteristic length scale by almost an order of magnitude (see Figure 6). When initiated over the summer or in ice free regions, surface eddies will be dissipated on a time scale of days once they encounter sea ice, as described in Section 3c. In contrast, halocline and deeper eddies, isolated from the ice cover by the strong stratification between water masses of different origin (see Figure 3), can grow independently of the presence of the ice.

Our numerical model results, presented in Figure 9, confirm the strong seasonality of the surface eddy field, and demonstrate that the entire Arctic Ocean's halocline shows signs of baroclinic instability, independently of the presence of sea ice.

We have additionally provided an explanation for how eddies generated within the energetic coastal currents can travel long distances if they are in the halocline. The strong stratification insulates subsurface eddies from the ice cover above without dissipating them (see Figure 8 for an example). At the same time, surface eddies originating within isopycnals outcropping in ice free regions can propagate under ice, providing a mechanism for, e.g., the transport of Pacific waters towards the interior, and the origin of the subsurface temperature maximum, into the halocline of the Canada basin (Spall et al. 2008; von Appen and Pickart 2011; Timmermans et al. 2017; Spall et al. 2018). Such transport would not be possible in the absence of a strong stratification close to the surface: moving at only a few centimeters per second, the eddies would be able to travel only a few tens of kilometers before being dissipated against the ice cover over a time scale of days.

Our analysis suggests how future changes in the ice cover and its seasonal variability will result in important changes in the Arctic Ocean eddy characteristics. In current conditions, the winter ice cover is strong and rough enough to prevent the growth of baroclinic instabilities close to the surface, thus blocking the main mechanism driving lateral mixing in the surface layer. The ice is therefore effectively shielded from intrusion of warm water from the side (Ramudu et al. 2018; Horvat et al. 2016). This would not be the case with thinner or smoother ice: less friction would result in a more active surface eddy field, even below ice. Consequences on the transport of heat below the ice, and on the regeneration of the ice cover the following winter, are to be expected.

Changes in stratification, observed in the past decade (e.g., Cole and Stadler 2019), are equally important and affect the vertical structure of the eddies and the interaction of halocline and deep eddies with the ice. For example, an erosion of the shallow peak in stratification, driven by an increase of momentum transfer from the atmosphere associated with a reduced ice cover, would result in the halocline eddies interacting with the ice itself, as shown in Figure 7.
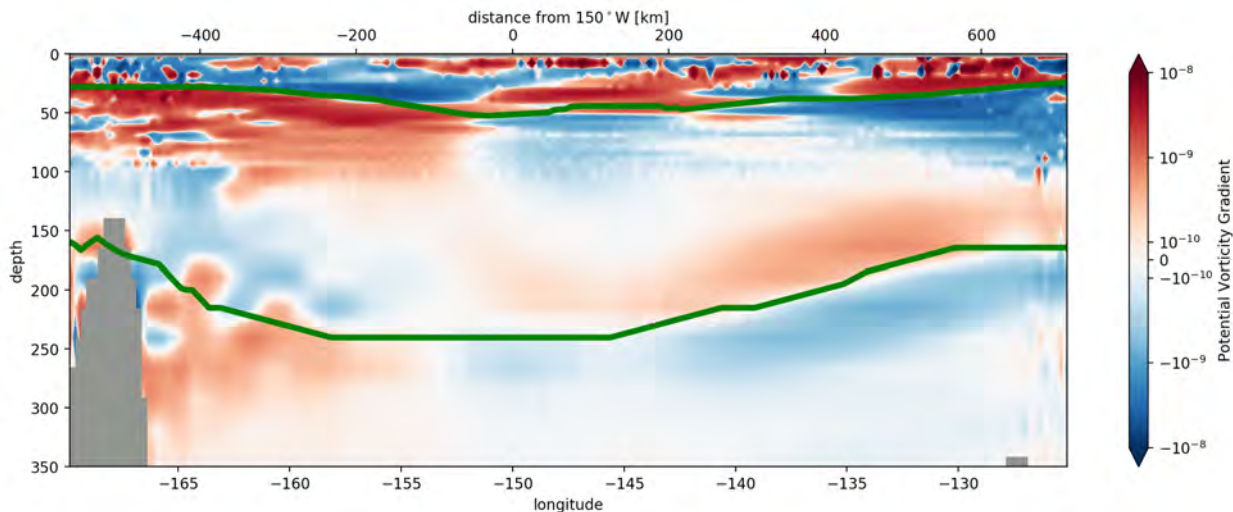
FIG. 10. Potential Vorticity gradient $\nabla \left(f \frac{\partial \rho}{\partial z} \right)$ across the Canada basin at 75°N (see black line in Figure 2). Its vertical inversion, extending all along the halocline supports the growth of halocline eddies independently of the presence of sea ice. Black lines mark the depth of the peaks in stratification visible in Figure 3. Data based on the 2005-2017 World Ocean Atlas climatology.

We have here provided a framework for the interpretation of the peculiarities of the eddy field in the Arctic, and confirmed our theoretical results using a high resolution pan-Arctic ocean model. More studies will be required to analyze the relationship between the sea ice state and the Ekman layer depth and the different regional characteristic of baroclinic instability across the Arctic, or to include a more accurate representation of the Ekman and mixed layer in the analysis. Additionally, the small scale eddies developing close to the surface, all-important for their interaction with sea-ice, will need to be parameterized in climate models for the foreseeable future, a problem that needs to be addressed by taking into account the large seasonal variability.

From the observational perspective, the top few meters closer to the surface, where a large part of the eddy activity and most of the variability take place, are not sampled by current moorings — which cannot extend to the surface because of the presence of ice — and only partially so by Ice Tethered Profilers (ITP) which are limited to depths larger than 7 m. This shallow region is also the location where we expect the largest impact of changes in sea-ice conditions. More innovative in-situ observations will provide very valuable information to further confirm our hypothesis, and inform the development and validation of models and parameterizations.

APPENDIX

References

Barcilon, V. (1964). Role of the Ekman Layers in the Stability of the Symmetric Regime Obtained in a Rotating Annulus. *Journal of the Atmospheric Sciences*, 21:291.

Brodeau, L., Barnier, B., Treguier, A. M., Penduff, T., and Gulev, S. (2010). An ERA40-based atmospheric forcing for global ocean circulation models. *Ocean Modelling*, 31(3-4):88–104.

Chao, S.-Y. Y. and Shaw, P.-T. T. (1996). Initialization, Asymmetry, and Spindown of Arctic Eddies. *Journal of Physical Oceanography*, 26(10):2076–2092.

Charney, J. G. (1947). The dynamics of long waves in a baroclinic westerly current. *Journal of Meteorology*, 4:135–163.
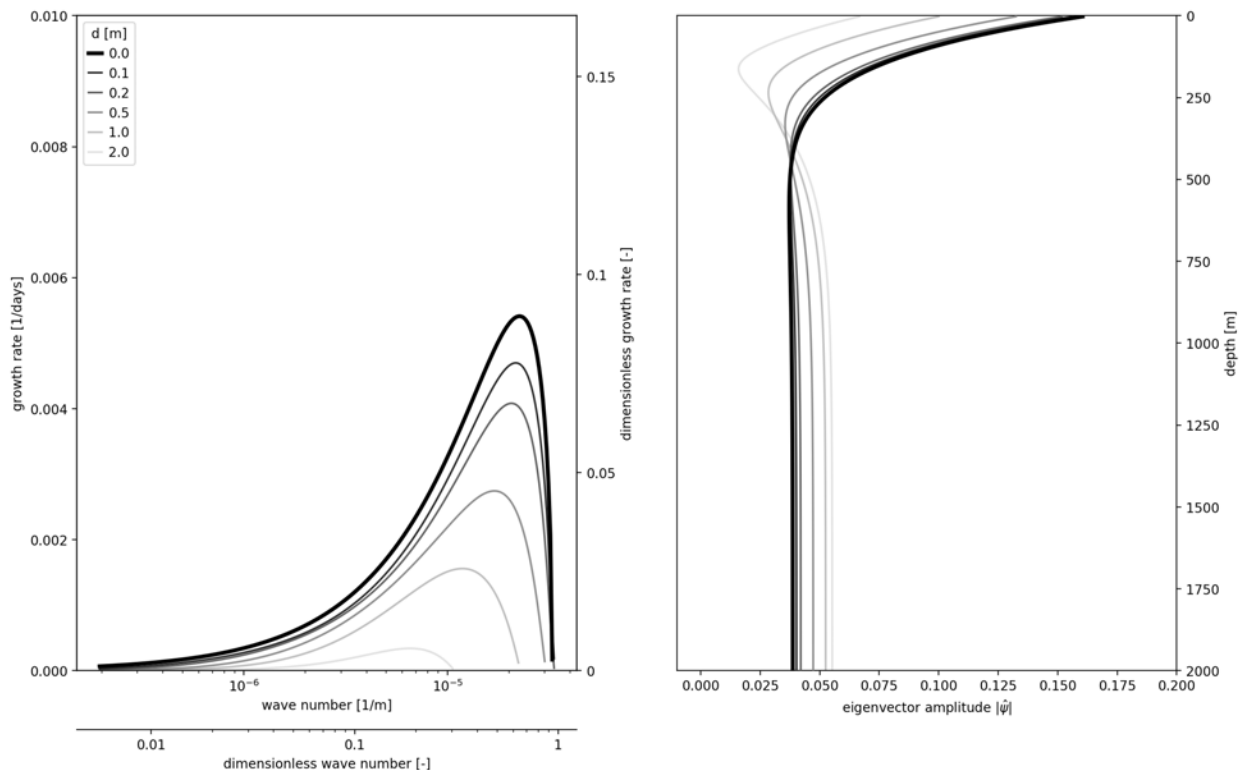
FIG. A1. Same as Figure 5, but for the Hunkins problem characterized by a stratification and velocity profiles both exponentially decaying with depth on a length scale of $h_\alpha = 200\,$m. The surface velocity is set to $U_s = 2\,$cm s^{-1}, the surface stratification to $N_s = 2 \times 10^{-2}\,$s^{-1}, and the total depth is set to $H = 2000\,$m, see Hunkins (1981) for details. The Ekman layer depth d is varied between $0\,$m and $2\,$m at both the surface and the ocean floor. Note that values on the vertical axis of the growth rate plot are ten times lower than in Figure 5, with the frictionless ($d = 0\,$m) case characterized by a time scale of order 200 days. Length scales, of order $100\,$km, are more than one order of magnitude larger than the observed ones. The scaling used to obtain the dimensionless growth rate and wave number are $\frac{f_0 U_s}{N_s h_\alpha}$ and $\frac{f_0}{N_s h_\alpha}$ respectively (compare with Figure 4 of Hunkins (1981)).

Charney, J. G. and Eliassen, A. (1949). A Numerical Method for Predicting the Perturbations of the Middle Latitude Westerlies. *Tellus*, 1(2):38–54.

Charney, J. G. and Stern, M. E. (1962). On the Stability of Internal Baroclinic Jets in a Rotating Atmosphere. *Journal of the Atmospheric Sciences*.

Cole, S. T. and Stadler, J. (2019). Deepening of the Winter Mixed Layer in the Canada Basin, Arctic Ocean Over 2006–2017. *Journal of Geophysical Research: Oceans*, pages 4618–4630.

Cole, S. T., Timmermans, M.-L., Toole, J. M., Krishfield, R. A., and Thwaites, F. T. (2014). Ekman Veering, Internal Waves, and Turbulence Observed under Arctic Sea Ice. *Journal of Physical Oceanography*, 44(5):1306–1328.

Cushman-Roisin, B. and Beckers, J.-M. (2010). *Introduction to Geophysical Fluid Dynamics. Physical and Numerical Aspects*, volume 101. Academic Press.

Dewey, S., Morison, J., Kwok, R., Dickinson, S., Morison, D., and Andersen, R. (2018). Arctic Ice-Ocean Coupling and Gyre Equilibration Observed With Remote Sensing. *Geophysical Research Letters*, 45(3):1499–1508.

Dupont, F., Higginson, S., Bourdallé-Badie, R., Lu, Y., Roy, F., Smith, G. C., Lemieux, J. F., Garric, G., and Davidson, F. (2015). A high-resolution ocean and sea-ice modelling system for the Arctic and North Atlantic oceans.

Eady, E. T. (1949). Long Waves and Cyclone Waves. *Tellus A*, 1:33–52.

Horvat, C., Tziperman, E., and Campin, J. M. (2016). Interaction of sea ice floe size, ocean eddies, and sea ice melting. *Geophysical Research Letters*, 43(15):8083–8090.

Hunke, E. C. and Dukowicz, J. K. (1997). An elastic–viscous–plastic model for sea ice dynamics. *Journal of Physical Oceanography*, 27(9):1849–1867.

Hunkins, K. L. (1974). Subsurface eddies in the Arctic ocean. *Deep-Sea Research*, 21:1017–1033.

Hunkins, K. L. (1981). Arctic Ocean eddies and baroclinic instability. Technical report, Lamont-Doherty Geol. Observ. of Columbia Univ.,, Palisades, N.Y.

Isachsen, P. E. (2011). Baroclinic instability and eddy tracer transport across sloping bottom topography: How well does a modified Eady model do in primitive equation simulations? *Ocean Modelling*, 39:183–199.
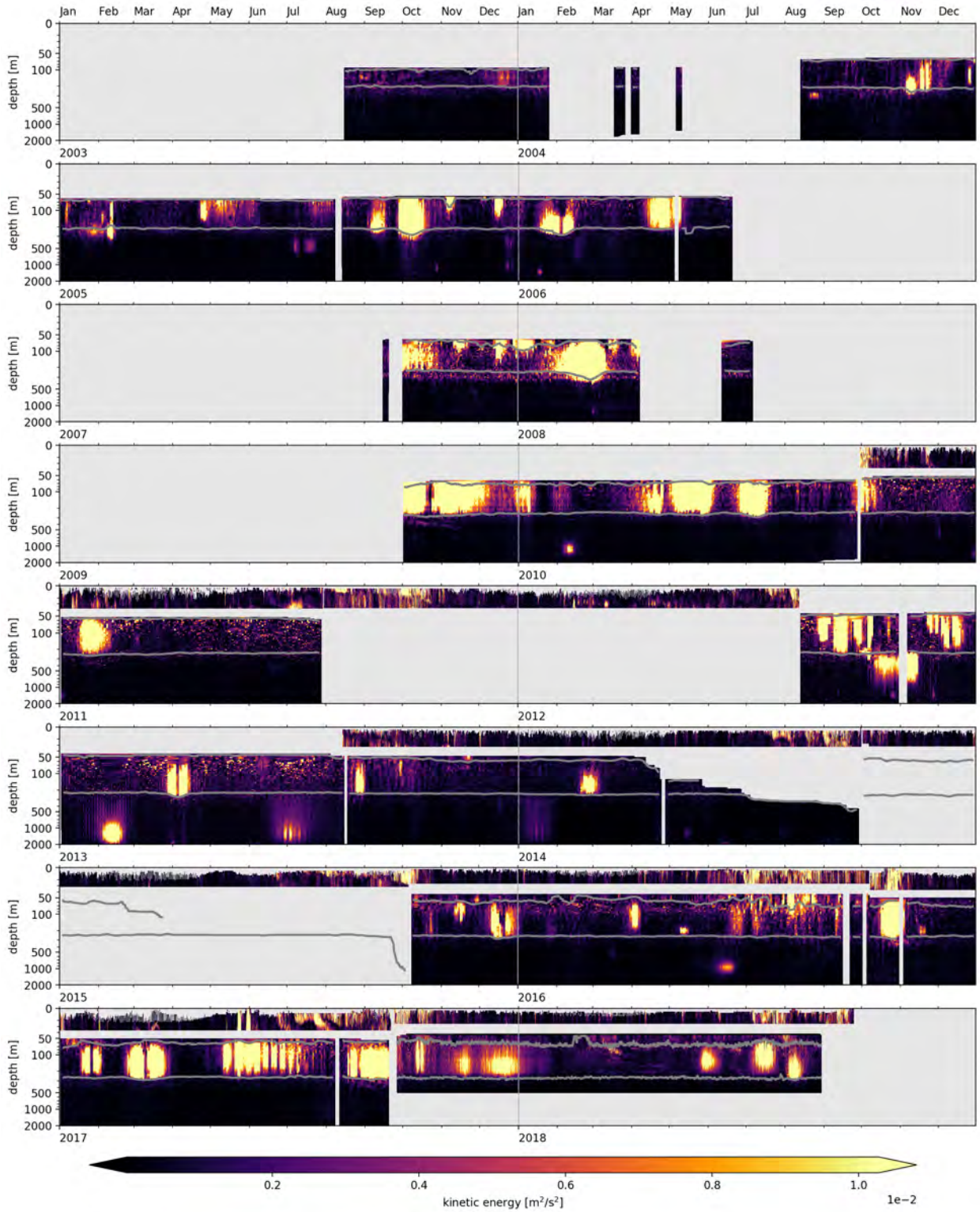
FIG. A2. Observed kinetic energy at mooring A, 2003-1018. Note that the vertical scale is linear until 50 m, and logarithmic thereafter. Gray lines mark peaks in stratification N^2.

Isachsen, P. E. (2015). Baroclinic instability and the mesoscale eddy field around the Lofoten Basin. *Journal of Geophysical Research: Oceans*, 120(4):2884–2903.

Kozlov, I. E., Artamonova, A. V., Manucharyan, G. E., and Kubryakov, A. A. (2019). Eddies in the Western Arctic Ocean From Spaceborne SAR Observations Over Open Ocean and Marginal Ice Zones. *Journal of Geophysical Research: Oceans*, 124(9):6601–6616.

Le Traon, P. (1991). Time scales of mesoscale variability and their relationship with space scales in the North Atlantic. *Journal of Marine Research*, 49(3):467–492.

Lique, C., Guthrie, J. D., Steele, M., Proshutinsky, A., Morison, J. H., and Krishfield, R. (2014). Diffusive vertical heat flux in the Canada Basin of the Arctic Ocean inferred from moored instruments. *Journal of Geophysical Research: Oceans*, 119(1):496–508.

MacGilchrist, G. A., Marshall, D. P., Johnson, H. L., Lique, C., and Thomas, M. (2017). Characterizing the chaotic nature of ocean ventilation. *Journal of Geophysical Research: Oceans*, 122(9):7577–7594.

Madec, G. and NEMO Team (2014). NEMO ocean engine. Technical Report 27, Institut Pierre-Simon Laplace (IPSL).

Manley, T. O. and Hunkins, K. (1985). Mesoscale Eddies of the Arctic Ocea. *Journal of Geophysical Research C Oceans*, 90(1974):4911–4930.

Manucharyan, G. E. and Isachsen, P. E. (2019). Critical Role of Continental Slopes in Halocline and Eddy Dynamics of the Ekman-Driven Beaufort Gyre. *Journal of Geophysical Research: Oceans*, 124(4):2679–2696.

Marshall, J., Jones, H., Karsten, R., and Wardle, R. (2002). Can Eddies Set Ocean Stratification? *Journal of Physical Oceanography*, 32(1):26–38.

Marta-Almeida, M., Ruiz-Villarreal, M., Pereira, J., Otero, P., Cirano, M., Zhang, X., and Hetland, R. D. (2013). Efficient tools for marine operational forecast and oil spill tracking. *Marine Pollution Bulletin*, 71(1-2):139–151.

McWilliams, J. C. (2008). The nature and consequences of oceanic eddies. In *Geophysical Monograph Series*, pages 5–15. American Geophysical Union (AGU).

Meneghello, G., Doddridge, E., Marshall, J., Scott, J., and Campin, J.-M. (2019). Exploring the role of the "Ice-ocean governor" and mesoscale eddies in the equilibration of the Beaufort Gyre: Lessons from observations. *Journal of Physical Oceanography*, 50:269–277.

Meneghello, G., Marshall, J., Campin, J.-M., Doddridge, E., and Timmermans, M.-l. (2018a). The Ice-Ocean Governor : Ice-Ocean Stress Feedback Limits Beaufort Gyre Spin-Up. *Geophysical Research Letters*, 45:11293—-11299.

Meneghello, G., Marshall, J., Cole, S. T., and Timmermans, M.-L. (2017). Observational inferences of lateral eddy diffusivity in the halocline of the Beaufort Gyre. *Geophysical Research Letters*, 44(24):12,331–12,338.

Meneghello, G., Marshall, J., Timmermans, M. L., and Scott, J. (2018b). Observations of seasonal upwelling and downwelling in the Beaufort Sea mediated by sea ice. *Journal of Physical Oceanography*, 48(4):795–805.

Newton, J. (1973). *The Canada Basin: Mean circulation and intermediate-scale flow features*. doctoral dissertation, University of Washington.

Newton, J. L., Aagaard, K., and Coachman, L. K. (1974). Baroclinic eddies in the Arctic Ocean. *Deep-Sea Research and Oceanographic Abstracts*, 21(9):707–719.

Nurser, A. J. G. and Bacon, S. (2014). The rossby radius in the arctic ocean. *Ocean Science*, 10(6):967–975.

Ou, H. W. and Gordon, A. L. (1986). Spin-down of baroclinic eddies under sea ice. *Journal of Geophysical Research*, 91(C6):7623.

Pedlosky, J. (1964). The Stability of Currents in the Atmosphere and the Ocean: Part I. *Journal of the Atmospheric Sciences*, 21(2):201–219.

Pedlosky, J. (1992). *Geophysical Fluid Dynamics*. Springer.

Phillips, N. A. (1954). Energy Transformations and Meridional Circulations associated with simple Baroclinic Waves in a two-level, Quasi-geostrophic Model. *Tellus*, 6:273–286.

Ramudu, E., Gelderloos, R., Yang, D., Meneveau, C., and Gnanadesikan, A. (2018). Large Eddy Simulation of Heat Entrainment Under Arctic Sea Ice. *Journal of Geophysical Research: Oceans*, 123(1):287–304.

Regan, H., Lique, C., Talandier, C., and Meneghello, G. (2020). Response of Total and Eddy Kinetic Energy to the recent spin up of the Beaufort Gyre. *Journal of Physical Oceanography*, 50:575–594.

Rousset, C., Vancoppenolle, M., Madec, G., Fichefet, T., Flavoni, S., Barthélemy, A., Benshila, R., Chanut, J., Levy, C., Masson, S., and Vivier, F. (2015). The Louvain-La-Neuve sea ice model LIM3.6: global and regional capabilities. *Geoscientific Model Development*, 8(10):2991–3005.

Smith, K. S. (2008). The geography of linear baroclinic instability in Earth's oceans. *Journal of Marine Research*, 65(5):655–683.

Spall, M. A., Pickart, R. S., Fratantoni, P. S., and Plueddemann, A. J. (2008). Western Arctic Shelfbreak Eddies: Formation and Transport. *Journal of Physical Oceanography*, 38(8):1644–1668.

Spall, M. A., Pickart, R. S., Li, M., Itoh, M., Lin, P., Kikuchi, T., and Qi, Y. (2018). Transport of Pacific Water Into the Canada Basin and the Formation of the Chukchi Slope Current. *Journal of Geophysical Research: Oceans*, 123:7453–7471.

Timmermans, M.-L., Marshall, J., Proshutinsky, A., and Scott, J. (2017). Seasonally derived components of the Canada Basin halocline. *Geophysical Research Letters*, 44(10):5008–5015.

Timmermans, M.-L., Toole, J. M., Proshutinsky, A., Krishfield, R., and Plueddemann, A. (2008). Eddies in the Canada Basin, Arctic Ocean, Observed from Ice-Tethered Profilers. *Journal of Physical Oceanography*, 38(1):133–145.

Timmermans, M.-L. L., Cole, S., and Toole, J. (2012). Horizontal Density Structure and Restratification of the Arctic Ocean Surface Layer. *Journal of Physical Oceanography*, 42(4):659–668.

Toole, J. M., Krishfield, R., Timmermans, M.-L., and Proshutinsky, A. (2011). The Ice-Tethered Profiler: Argo of the Arctic. *Oceanography*, 24(3):126–135.

Trodahl, M. and Isachsen, P. E. (2018). Topographic influence on baroclinic instability and the mesoscale eddy field in the northern North

Atlantic ocean and the Nordic seas. *Journal of Physical Oceanography*, 48(11):2593–2607.

Tulloch, R., Marshall, J., Hill, C., and Smith, K. S. (2011). Scales, Growth Rates, and Spectral Fluxes of Baroclinic Instability in the Ocean. *Journal of Physical Oceanography*, 41(6):1057–1076.

Våge, K., Pickart, R. S., Pavlov, V., Lin, P., Torres, D. J., Ingvaldsen, R., Sundfjord, A., and Proshutinsky, A. (2016). The Atlantic Water boundary current in the Nansen Basin: Transport and mechanisms of lateral exchange. *Journal of Geophysical Research: Oceans*, 121(9):6946–6960.

von Appen, W.-J. and Pickart, R. S. (2011). Two Configurations of the Western Arctic Shelfbreak Current in Summer. *Journal of Physical Oceanography*, 42(3):329–351.

Watanabe, E., Onodera, J., Harada, N., Honda, M. C., Kimoto, K., Kikuchi, T., Nishino, S., Matsuno, K., Yamaguchi, A., Ishida, A., and Kishi, M. J. (2014). Enhanced role of eddies in the Arctic marine biological pump. *Nature Communications*, 5:3950.

Williams, G. P. and Robinson, J. B. (1974). Generalized Eady Waves with Ekman Pumping. *Journal of the Atmospheric Sciences*, 31(7):1768–1776.

Wunsch, C. (2002). Ocean observations and the climate forecast problem. *International Geophysics*, 83(C):233–245.

Zhao, M. and Timmermans, M. L. (2015). Vertical scales and dynamics of eddies in the Arctic Ocean's Canada Basin. *Journal of Geophysical Research: Oceans*, 120(12):8195–8209.

Zhao, M., Timmermans, M.-L., Cole, S. T., Krishfield, R., Proshutinsky, A., and Toole, J. M. (2014). Characterizing the eddy field in the Arctic Ocean halocline. *Journal of Geophysical Research: Oceans*, 119(12):8800–8817.

Zhao, M., Timmermans, M.-L., Cole, S. T., Krishfield, R., and Toole, J. M. (2016). Evolution of the eddy field in the Arctic Ocean's Canada Basin, 2005-2015. *Geophysical Research Letters*, 43(15):8106–8114.

Zhao, M., Timmermans, M.-L., Krishfield, R., and Manucharyan, G. E. (2018). Partitioning of Kinetic Energy in the Arctic Ocean's Beaufort Gyre. *Journal of Geophysical Research: Oceans*, 123(7):4806–4819.

Zhong, W., Steele, M., Zhang, J., and Zhao, J. (2018). Greater Role of Geostrophic Currents in Ekman Dynamics in the Western Arctic Ocean as a Mechanism for Beaufort Gyre Stabilization. *Journal of Geophysical Research: Oceans*, 123(1):149–165.